Contents lists available at ScienceDirect

Physics of the Earth and Planetary Interiors

Buoyancy, bending, and seismic visibility in deep slab stagnation

Craig R. Bina [a,*], Hitoshi Kawakatsu [b]

[a] *Department of Earth and Planetary Sciences, Northwestern University, 1850 Campus Drive, Evanston, IL 60208-2150, USA*
[b] *Earthquake Research Institute, University of Tokyo, 1-1-1 Yayoi, Bunkyo-ku, Tokyo 113-0032, Japan*

ABSTRACT

The petrological consequences of deep subhorizontal deflection ("stagnation") of subducting slabs should affect both apparent seismic velocity structures and slab morphology. We construct kinematic thermal models of stagnant slabs and perform thermodynamic modeling of the consequent perturbation of high-pressure phase transitions in mantle minerals, focusing upon Japan as our study area. We calculate associated thermo-petrological buoyancy forces and bending moments which (along with other factors such as viscosity variations and rollback dynamics) may contribute to slab deformation. We consider effects of variations in depth of stagnation, post-stagnation dip angle, phase transition sharpness, transition triplication due to multiple intersection of geotherms with phase boundaries, and potential persistence of metastable phases due to kinetic hindrance. We also estimate seismic velocity anomalies, as might be imaged by seismic tomography, and corresponding seismic velocity gradients, as might be imaged by receiver-function analysis. We find that buoyant bending moment gradients of petrological origin at the base of the transition zone may contribute to slab stagnation. Such buoyancy forces vary with the depth at which stagnation occurs, so that slabs may seek an equilibrium slab stagnation depth. Metastable phase bending moment gradients further enhance slab stagnation, but they thermally decay after ∼600–700 km of horizontal travel, potentially allowing stagnant slabs to descend into the lower mantle. Stagnant slabs superimpose zones of negative velocity gradient onto a depressed 660-km seismic discontinuity, affecting the seismological visibility of such features. Seismologically resolvable details should depend upon both stagnation depth and the nature of the imaging technique (travel-time tomography vs. boundary-interaction phases). While seismic tomography appears to yield images of stagnant slabs, discontinuity topography beneath Japan resolved by migrated receiver functions appears to be consistent with slab penetration of the transition zone. However, model slabs which bottom around ∼780–810 km and then bend upwards by a few degrees can match both the tomographic and receiver-function images.

© 2010 Elsevier B.V. All rights reserved.

1. Introduction

Many subducting slabs appear to "stagnate", or bend toward the horizontal, near the base of the transition zone (Fukao et al., 2001, 2009). Evidence for such slab stagnation can be found in a variety of observations: in correlations between patterns of past subduction and fast seismic velocity anomalies in the mantle (Čížková et al., 1998), in subhorizontal deflections of fast velocity anomalies in P- and S-wave seismic tomography (Widiyantoro et al., 1999; Fukao et al., 2001; Sugioka et al., 2010), and in the shallowing of apparent dip angles exhibited by Wadati-Benioff patterns of slab seismicity (Chen et al., 2004, 2005). Such deep subhorizontal extensions of subduction – or "stagnant slabs" – constitute unusual thermobaric environments, in that subducted material may gradually undergo nearly isobaric thermal assimilation. The petrological

consequences, in terms of equilibrium or metastable phase relations, should affect both slab morphology and apparent seismic velocity structures.

Here we adopt a simple kinematic approach and focus primarily upon the role of thermo-petrological buoyancy forces (Yoshioka et al., 1997; Tetzlaff and Schmeling, 2000; Bina et al., 2001) in the stagnant slab environment, both in terms of the generation of buoyant bending moments within the slab and in terms of local perturbation of seismic velocity structures. Other studies have addressed additional factors in the framework of dynamical simulations. For example, the interplay between buoyancy forces, trench rollback, and viscosity contrasts has been addressed by Christensen (2001) and Torii and Yoshioka (2007). Interactions between slab rollback, grain-size reduction, and limiting yield stress have been studied by Čížková et al. (2002), and the effect of slab thermal history on resistance to buoyant bending has been analyzed by Čížková et al. (2007). Furthermore, Torii and Yoshioka (2007) have modeled viscosity effects in the limit of vanishingly small Clapeyron slopes. Billen (2008) has reviewed the interplay of many of these dynamical effects.

Beyond the well-known thermal dependence of buoyancy forces upon subduction rate, dip angle, and lithospheric age (Kirby et al., 1996; Yoshioka et al., 1997; Tetzlaff and Schmeling, 2000; Bina et al., 2001), we focus on slab bending moments, the role of slab stagnation depth and post-stagnation geometry, seismological visibility, and reconciliation of receiver-function images with tomographic images. Our goal here is not to reproduce slab behavior in all its complexity but rather to elucidate the signs, relative magnitudes, and implications for seismological imaging of various fundamental buoyancy-related phenomena associated with phase relations in stagnant slabs.

2. Methods

We begin by calculating slab thermal models using the kinematic finite-difference heat-transfer algorithm *TEMSPOL* (Negredo et al., 2004), expanded to include the lower mantle and estimated P-wave velocity anomalies (Negredo, pers. comm., 2005), and modified by us to allow prescribed changes in slab dip angles at depth. As our primary study area lies beneath Japan – generally along a profile from (30°N, 129°E) to (36°N, 144°E) – we adopt thermal parameters appropriate for this region: 130 Ma lithosphere, 9 cm/yr convergence, and 45° dip angle, yielding a slab thermal parameter Φ of 8270 m (Kostoglodov, 1989; Kirby et al., 1991, 1996; Gorbatov and Kostoglodov, 1997). Slabs are advanced using time-steps of 25 Myr along a spatial grid with 5-km spacing. (Differences in the treatment of induced-flow effects result in minor differences between thermal models constructed using the *TEM-SPOL* algorithm and those using the Minear–Toksöz–Sleep–Stein algorithm (Minear and Toksöz, 1970; Kirby et al., 1996; Bina et al., 2001); in *TEMSPOL* calculations slabs remain somewhat colder so that the 1000 K isotherm approximating the limit of metastability falls slightly closer to the slab surface.)

Using these slab thermal models, we calculate equilibrium phase relations in olivine of Fo_{90} composition (Fig. 1) by the technique of free-energy minimization for the internally consistent thermodynamic model of Fei et al. (1991) using the simulated annealing method of Bina (1998a), as in previous subduction studies (Bina et al., 2001). For comparative purposes, we also calculate phase relations using the simplified equilibrium phase diagram of Schmeling et al. (1999). We address the possibility of metastable persistence of olivine (Green and Zhou, 1996; Kirby et al., 1996; Chen et al., 2008; Kubo et al., 2008) using the simplified thermokinetics of Schmeling et al. (1999) as well as those (based on an isothermal reaction threshold of 1000 K) of Bina et al. (2001).

From the resulting phase proportions and compositions we calculate densities for each mineral assemblage which, when multiplied by gravitational acceleration, allow the mapping of spatial variations in buoyancy forces. Such buoyancy forces may be decomposed into two orthogonal components. The slab-parallel component $f_{\parallel}$ contributes primarily to the down-dip stress field in the slab and has been the focus of previous studies (Bina et al., 2001). The slab-normal component $f_{\perp}$, on the other hand, contributes primarily to bending moments (Karato et al., 1998; Brocher et al., 2001) acting upon the slab.
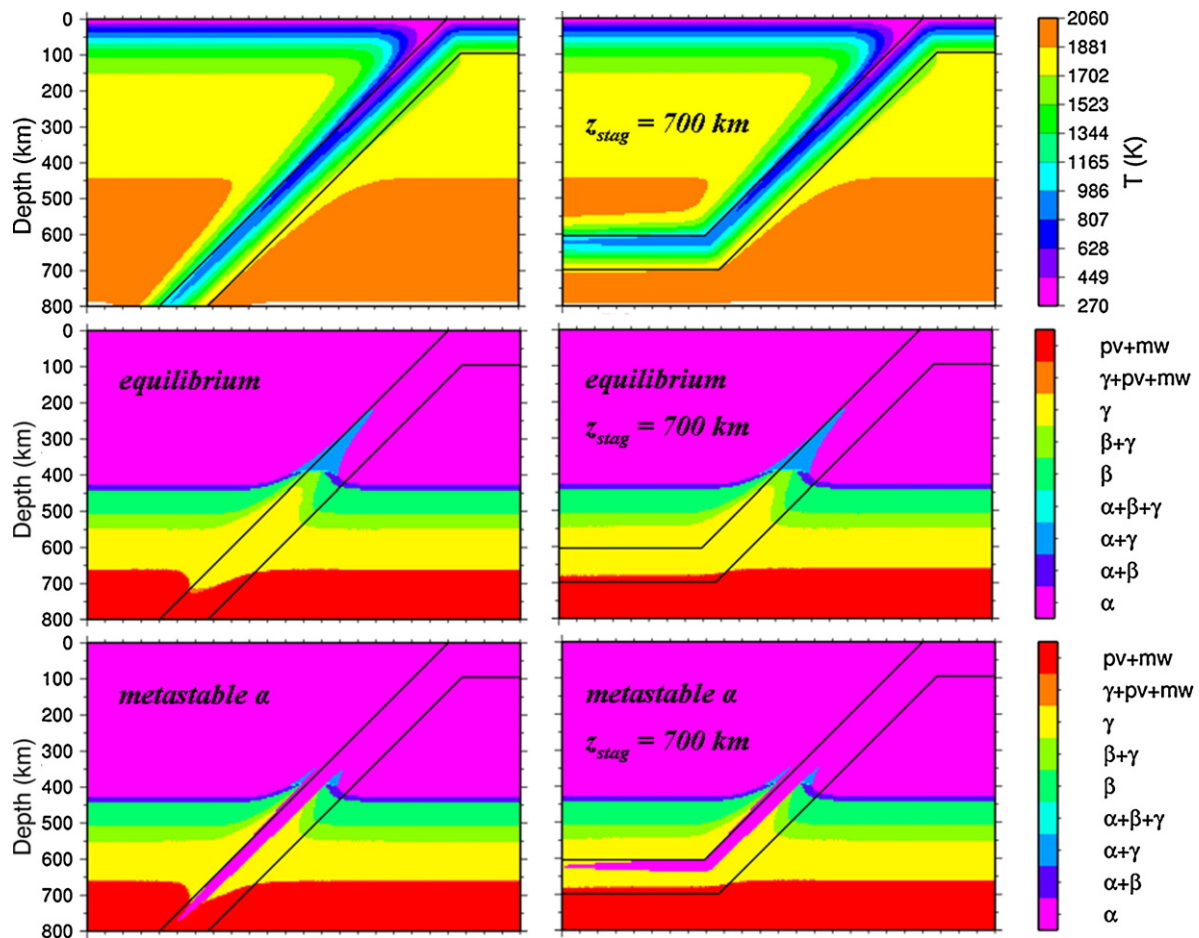

Fig. 1. Calculated thermal models (top) for penetrative (left) and stagnant (right, z_{stag} = 700 km) slabs. Corresponding equilibrium (middle) and disequilibrium (bottom) phase assemblages.
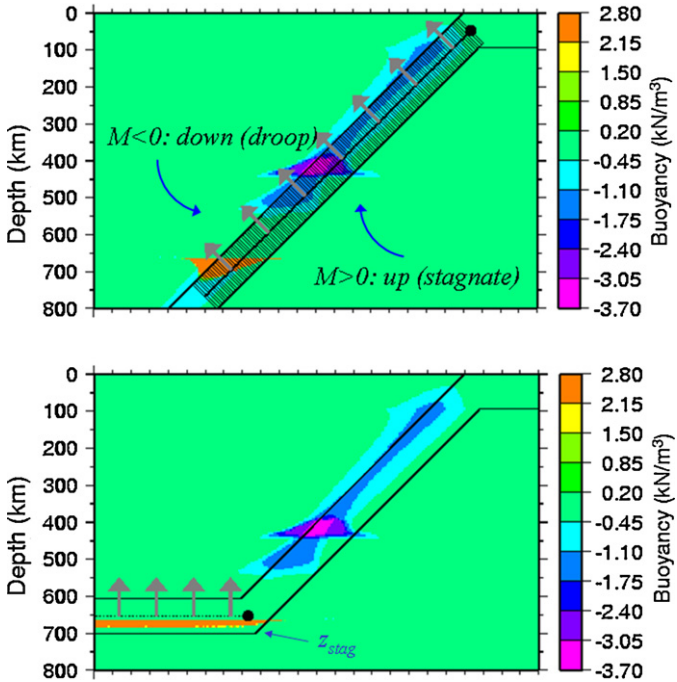
Fig. 2. Calculation $[M = \int f_\perp(x) \cdot x \cdot dx]$ of slab bending moments about trench axis (top) and stagnation axis (bottom). Solid circle denotes bending moment axis; arrows indicate slab-normal component of thermo-petrological buoyancy forces (background colors).

3. Bending moments

We calculate buoyant bending moments M by integrating down the slab the product of the slab-normal component of buoyancy force and the distance from the bending moment axis (Fig. 2), adopting the sign convention in which $M > 0$ corresponds to a moment tending to bend the slab upward toward the horizontal (i.e., one promoting slab stagnation). As these bending moments are calculated using buoyancy forces per unit volume, they technically are bending moment densities.

For $\quad f_\perp(r) = g \cos\delta \int \int_{B(r)} [\rho(x, z) - \rho_m(z)] \, dx \, dz / \int \int_{B(r)} dx \, dz$, we find the bending moment density $M(s) = \int_0^s f_\perp(r) \cdot r \cdot dr$, where r and s are distance down the midline of the dipping slab from the bending moment axis, g is the local gravitational acceleration, δ is the dip angle of the slab, $\rho(x, z)$ is the density of the mineral assemblage at a grid point, $\rho_m(z)$ is the reference mantle density (far from the slab) at depth z, and $B(r)$ is the rectangular region with centroid located at distance r down the midline of the dipping slab from the bending moment axis whose long axis (of length 95 km) is normal to the midline and whose short axis (1–5 km) depends upon the grid spacing.

The bending moment axis is initially set within the slab at the trench (the "trench axis"), but as the slab may potentially bend around axes at a variety of depths, the gradient of the bending moment density, $\nabla M(s) = f_\perp(s) \cdot s$, equivalent to torque due to local buoyancy, may be a more useful indicator of driving forces for slab stagnation. Essentially, M and ∇M represent two end-member cases, the former for a strictly rigid slab and the latter for a very soft slab, whereas the behavior of a "real" physical slab should be intermediate between these two extremes.

Calculation of bending moments and their gradients for both equilibrium and disequilibrium cases reveals several interesting features (Fig. 3). Firstly, the bending moment density gradient is maximized at the base of the transition zone, near 700 km depth, suggesting this area as the likely locus of slab stagnation, as seen in
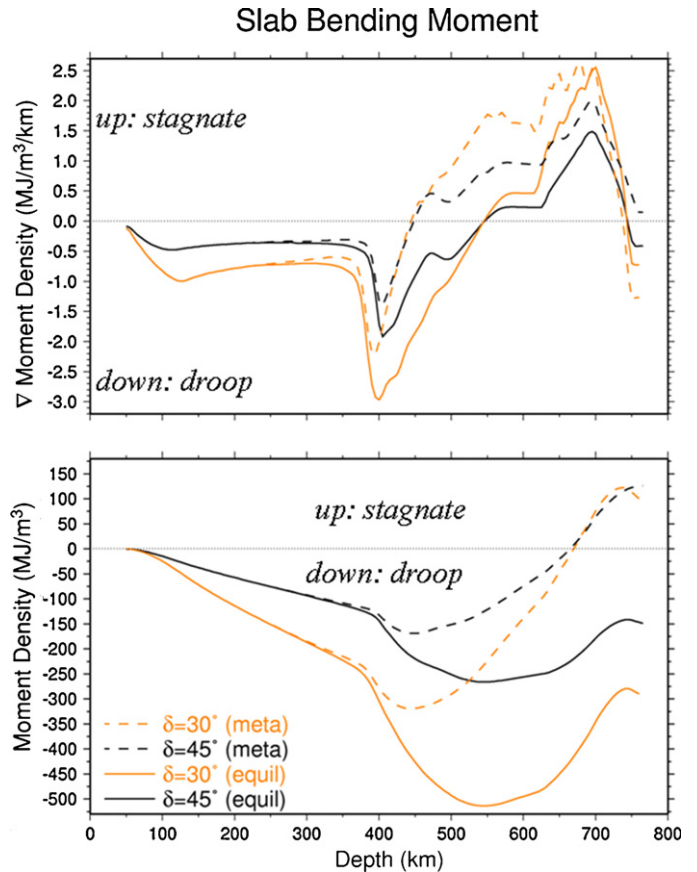

Fig. 3. Bending moment densities about trench axis and their gradients for equilibrium (solid) and disequilibrium (dashed) cases, for both 45° (black) and smaller 30° (orange) dip. Note extrema in gradients near 700 km and 400 km depth. Moments and gradients are larger in magnitude at smaller dip angles and more positive in cases of metastable persistence. (For interpretation of the references to color in this figure legend, the reader is referred to the web version of the article.)

some seismicity profiles (e.g., profiles *Izu2*, *Ind2*, *Van2*, and *Ton1* of Chen et al. (2004, 2005)). Secondly, varying the dip angle from 45° to 30° unsurprisingly confirms that bending moments and their gradients are larger in magnitude at smaller dip angles. To the extent that buoyant bending moments (as opposed to viscosity contrasts, for example) contribute to slab stagnation, this suggests that stagnation near 700 km depth may be more likely for initially shallowly dipping slabs. Thirdly, the bending moment density gradient is minimized, with a negative value, near 400 km depth. This suggests a driving force for possible increases in slab dip, or "slab drooping", below depths of 300 km, as observed in some seismicity profiles (e.g., profiles *SA6*, *SA7*, *Izu2*, *Mar*, *Ind2*, and *Ind3* of Chen et al. (2004, 2005)). In light of dip-dependence, this suggests a greater potential for such slab drooping in initially shallowly dipping slabs. Fourthly, bending moments and their gradients are more positive in cases of metastable persistence. Indeed, the absolute bending moment exhibits a crossover from negative to positive (i.e., stagnating) around 700 km depth in such cases (as does bulk slab buoyancy (Bina et al., 2001)). This suggests a greater potential for stagnation in colder slabs which are more likely to exhibit disequilibrium mineralogy.

Having reviewed the nature of buoyant bending moments which may be expected to affect slab morphology, we next examine how such bending moments should vary with the depth of slab stagnation. To this end, we define the stagnation depth z_{stag} as the depth of the bottom of the stagnant slab. Shifting the bending axis to within the slab at the depth of stagnation (the "stagnation axis"), we calculate buoyancy anomalies (Fig. 4) as well as
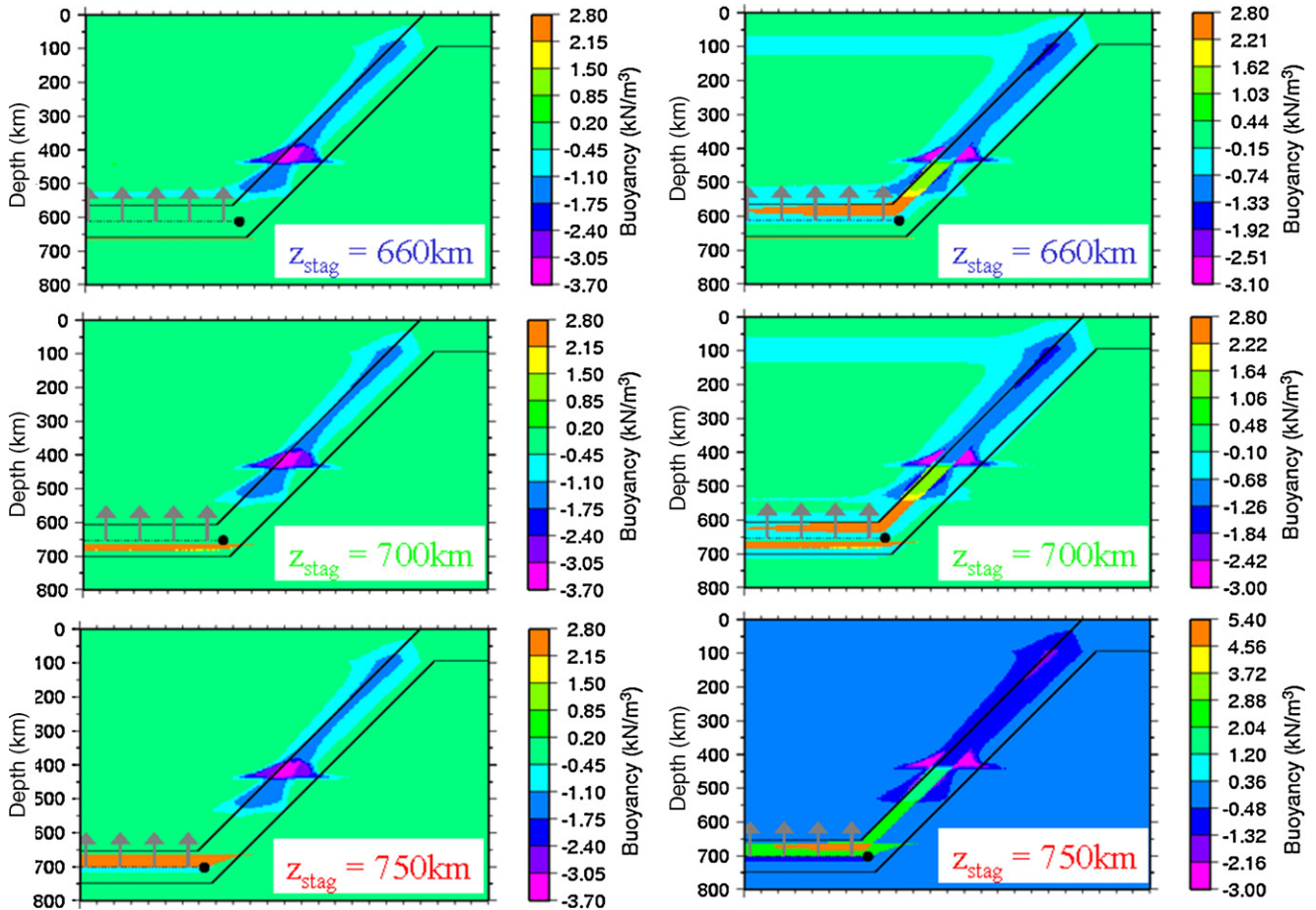
Fig. 4. Thermo-petrological buoyancy forces for varying depths of slab stagnation (z_{stag} = 660 km, 700 km, 750 km), for equilibrium (left) and metastable (right) cases. Note large buoyancies requiring change of scale for metastable z_{stag} = 750 km case.

bending moment densities and their gradients (Fig. 5), in both equilibrium and disequilibrium mineralogies, for cases in which z_{stag} is 660 km, 700 km, or 750 km. For shallower z_{stag}, bending moments and their gradients tend to bend slabs downwards; for deeper z_{stag}, bending moments and their gradients tend to bend slabs upwards, increasingly so for larger z_{stag}. This suggests the existence of an equilibrium 660 km $< z_{stag} <$ 700 km. Because of the simple geometric dip-dependence which generates larger buoyant bending moments at smaller dip angles, subducting slabs may overshoot their equilibrium z_{stag} before subsequently rebounding.

In cases of continuation of metastable persistence into the recumbent slab, the effects of metastability on bending-moment behavior are substantial. Bending moments tend to bend slabs upwards over the entire range of stagnation depths in cases of metastable persistence. However, unlike the essentially constant bending moment gradients in the equilibrium case, in the disequilibrium case bending moment gradients tend to deform slabs upwards only until ~600–700 km of horizontal travel have been achieved, due to gradual thermal equilibration and consequent decay of positive buoyancy anomalies. (Thermal equilibration may be enhanced by anomalous latent heat release associated with disequilibrium transformation of metastable material (Bina, 1998b), but these effects are not included in this simple model.) Thereafter, bending moment gradients become consistent with downward deflection. Thus, such lateral decay of buoyancy forces would allow stagnant slabs eventually to be drawn into the lower mantle.

This analysis of buoyant bending moments is intended to elucidate patterns of phase-transition buoyancy contributions to slab stagnation. As noted above, additional dynamical effects, such as

variations in viscosity structure and trench retreat behavior, may also contribute to slab stagnation.

4. Seismological visibility

Next we examine how the seismological visibility of stagnant slabs may vary with the depth of slab stagnation, as viewed through two different approaches. Firstly, using Voigt–Reuss–Hill averaging of elastic moduli for mineral assemblages, we calculate perturbations in bulk sound velocity δV_{Φ} relative to a reference model (which in this case is simply the slab-free, far right-hand edge of the mantle model), for equilibrium mineralogy, in an effort to approximate the view that might be formed through seismic tomography (Fig. 6). In this case, the broad, fast anomaly associated with the recumbent portion of the slab is damped and thinned at larger z_{stag}, because the reference model in the subtrahend has become faster below 660 km (due to equilibrium onset of the $rw \rightarrow pv + mw$ reaction) while the slab model in the minuend has not become faster below 660 km (due to equilibrium onset of the reaction at higher pressures within the cold slab thermal environment). Thus, greater stagnation depths may be expected to reduce the apparent velocity anomaly associated with the slab as imaged through seismic tomography.

Secondly, we calculate the vertical gradient in bulk sound velocity $\partial V_{\Phi}/\partial z$ (technically, the *fractional* vertical velocity gradient, $V_{\Phi}^{-1} \cdot \partial V_{\Phi}/\partial z$, which normalizes the gradient to the local velocity), in an effort to approximate the view that might be formed through study of reflected and converted seismic phases (Fig. 7). In this case, larger z_{stag} is associated with greater depression of the equilibrium
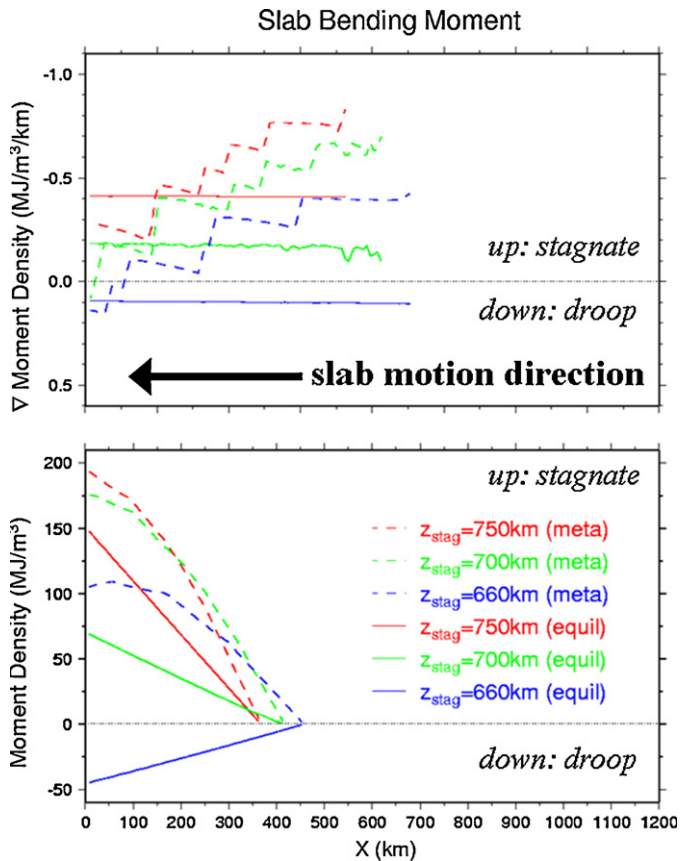
Slab Bending Moment

Fig. 5. Bending moment densities about stagnation axis and their gradients for equilibrium (solid) and disequilibrium (dashed) cases, for varying depths of slab stagnation (z_{stag} = 660 km, 700 km, 750 km). Note decay of metastable gradients due to gradual thermal equilibration. (Slab motion is leftward in the negative-x direction, so sign convention for gradients is reversed. Stair-step pattern for metastable gradients is an artifact of spatial granularity in integration and differentiation along horizontal axis.)

Fig. 6. Calculated perturbations in bulk sound velocity δV_Φ relative to a reference model, to approximate imaging by seismic tomography, for varying depths of slab stagnation (z_{stag} = 660 km, 700 km, 750 km). Note damping of slab anomaly at larger z_{stag}, as reference model grows faster immediately below 660 km while the slab model does not.

$rw \rightarrow pv + mw$ reaction (due to low slab temperatures) as well as a slight decrease in the sharp velocity gradient accompanying this reaction (due to its superposition upon a negative velocity gradient within the slab, as noted below). Both the vertical and lateral extent of downward deflection of the equilibrium $rw \rightarrow pv + mw$ transition exhibit dependence upon stagnation depth. Small values of z_{stag} (e.g., 660 km) yield shallow and broad depressions of the phase boundary, while larger values (e.g., 750 km) produce deep and broad depressions. Still larger values (e.g., $\geq$ 800 km) yield deep and narrow depressions similar to those expected for direct slab penetration. Note that $\partial V_\Phi / \partial z < 0$ within the body of the recumbent slab, because necessarily $\partial T/\partial z \gg 0$ where the cold slab lies atop warmer mantle, so that a sharp positive velocity gradient underlies a broader negative velocity gradient at intermediate (e.g., 700 km) stagnation depths. The superposition of this broad negative (vertical) velocity gradient upon the sharper $rw \rightarrow pv + mw$ transition should affect the seismological visibility of the latter.

While the immediately preceding discussion of $\partial V_\Phi / \partial z$ is largely relevant to seismic studies of reflected and converted phases which interact with boundaries at subvertical incidence, the picture may be broadened to arbitrary angles by examining the magnitudes of velocity gradients $\left| \nabla V_\Phi \right|$. Such a calculation for the case of metastably persisting olivine, for example, shows that the nearly isothermal and essentially univariant boundaries of a putative wedge of metastable olivine are potentially more reflective than either of the main transition zone seismic discontinuities (Fig. 8).
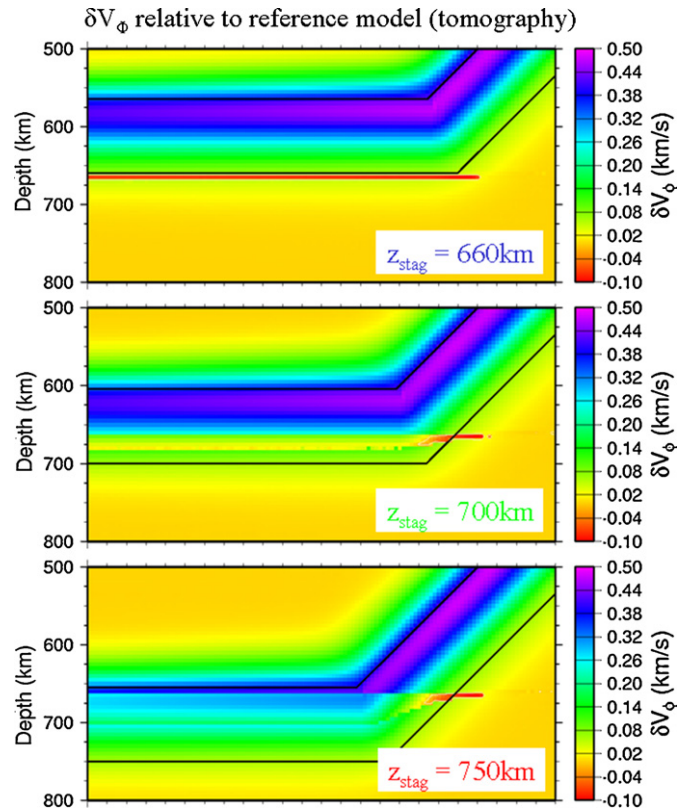
Such steeply dipping sharp velocity gradients may be seismologically observable (Kawakatsu, 2008).

5. Receiver-function interpretation

Seismological constraints on the thermal structure of the subducting slab beneath our study area in Japan are provided by migrated receiver functions and body-wave tomography (Fig. 9). P- and S-wave seismic tomography in this region produce images featuring broad subhorizontal deflections of fast velocity anomalies within the transition zone indicative of slab stagnation (Fukao et al., 2001; Sugioka et al., 2010). On the other hand, images derived from migrated receiver functions from Hi-net data (Kawakatsu and Watada, 2005) yield high-resolution constraints on the lateral depth variations of the 660-km seismic discontinuity beneath Japan (Bina and Kawakatsu, 2006) along this apparently stagnant slab. The receiver functions reveal the location of a sharp S-wave velocity increase (evidenced by continuous warm colors between depths of ~650 km and ~720 km) which correspond to a depressed 660 km discontinuity whose deepest point nearly corresponds to the deepest extent of the high-velocity anomaly in the tomographic images.

Assuming that this discontinuity topography represents equilibrium deflection of the $rw \rightarrow pv + mw$ transition (neglecting potential kinetic hindrance (Kubo et al., 2002) of the transition), the observed topography suggests a large but relatively narrow cold anomaly where the slab first intersects the lower mantle. Thus, migrated receiver-function images of this region appear to be consistent with a classic dipping slab, with an uplifted "410 km" and a depressed "660 km" discontinuity arising from δT of $\lesssim 1000°$ C as estimated from Clapeyron slopes of Bina and Helffrich (1994),
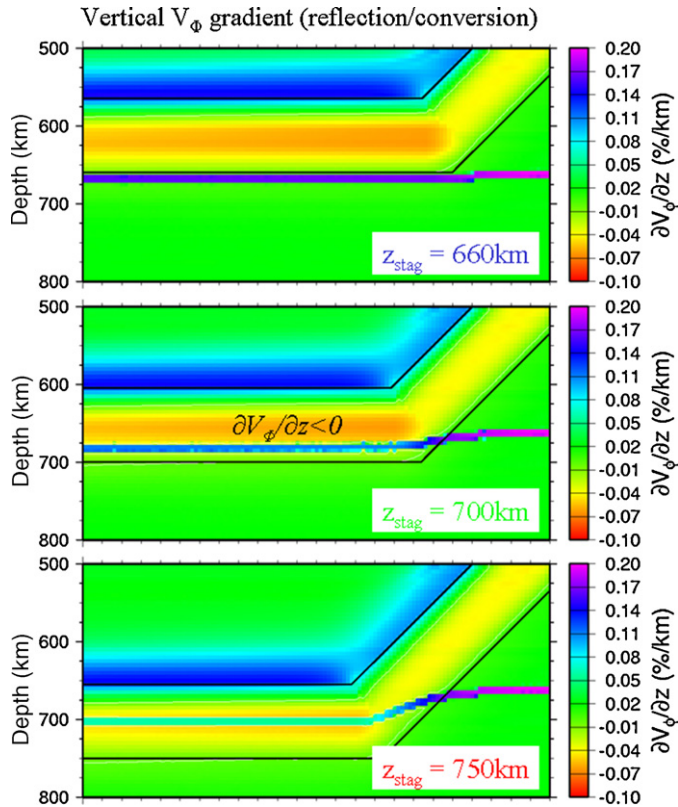
Fig. 7. Calculated (fractional) vertical gradients in bulk sound velocity $\partial V_\Phi/\partial z$, to approximate imaging by seismic reflections and conversions, for varying depths of slab stagnation (z_{stag} = 660 km, 700 km, 750 km). Note z_{stag}-dependence of $rw \rightarrow pv + mw$ equilibrium deflection. Note also broad negative velocity gradient ($\partial V_\Phi/\partial z < 0$) within recumbent slab (as cold slab lies atop warmer mantle), superposition of which affects seismological visibility of sharp $rw \rightarrow pv + mw$ transition.
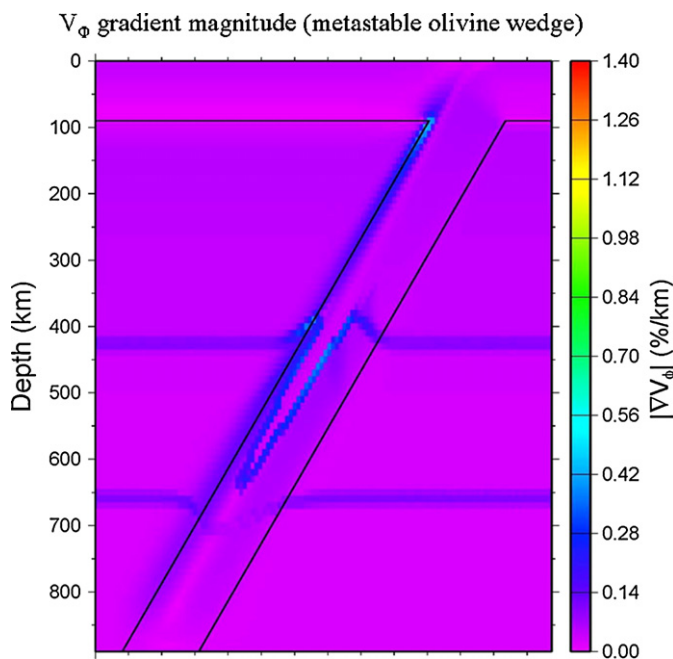

Fig. 8. Calculated magnitudes of bulk sound velocity gradients $|\nabla V_\Phi|$ for a case of metastably persisting olivine. Note that nearly isothermal and essentially univariant boundaries of putative metastable wedge are potentially more reflective than main transition zone seismic discontinuities.
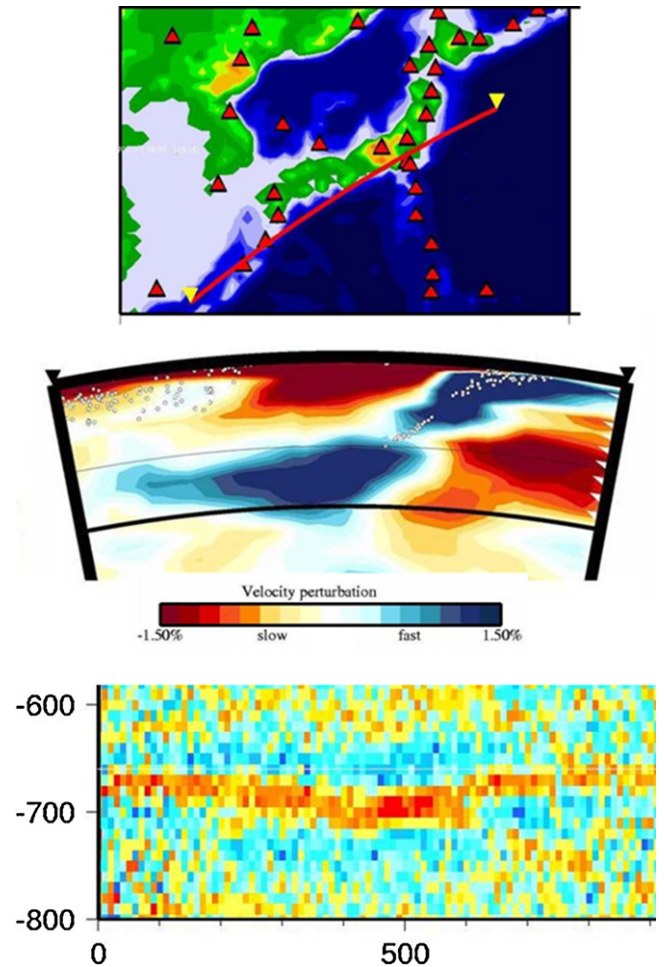

Fig. 9. Seismological images beneath Japanese study area [top]. P-wave tomography *WEPP2* (middle, Fukao et al., 2001) shows fast anomaly of stagnant slab in transition zone; thin and thick horizontal lines indicate nominal 410 km and 660 km discontinuities, respectively. Migrated receiver functions (bottom, Kawakatsu and Watada, 2005; Bina and Kawakatsu, 2006) resolve lateral depth variations of seismic reflectors; continuous warm colors (red, yellow) between depths of ~650 km and ~720 km indicate locations of sharp S-velocity increase corresponding to depressed 660 km discontinuity, whose deepest point nearly corresponds to that of the high-velocity anomaly in the tomographic image. (For interpretation of the references to color in this figure legend, the reader is referred to the web version of the article.)

although this topography has also been modeled using smaller Clapeyron slopes in combination with kinetic effects (Kawakatsu, 2008).

Reconciling these two distinct sets of observations can be problematic, as can be gleaned from our models (Fig. 10) for both a slab which penetrates through the transition zone undeflected and a slab which stagnates at a depth of 700 km. Penetrative slabs exhibit deep depression of the $rw \rightarrow pv + mw$ transition below 660 km, with swift rebound back to 660 km depth beyond the slab thermal halo. In the penetrative case, deep deflection of "660-km" discontinuity matches the migrated receiver functions reasonably well (although the receiver functions exhibit somewhat broader depression), but the inclined pattern of P-wave velocity anomalies does not match the recumbent pattern in the tomographic images. On the other hand, stagnant slabs exhibit moderate depression of the $rw \rightarrow pv + mw$ transition below 660 km, with significantly spatially delayed rebound back to 660 km depth. In the stagnant case, recumbent patterns of fast P-wave velocity anomalies match the tomographic images, but rebound of the deflected "660-km" discontinuity is delayed to too great an extent to match the migrated receiver functions. Rebound of the "660" grows sufficiently swift
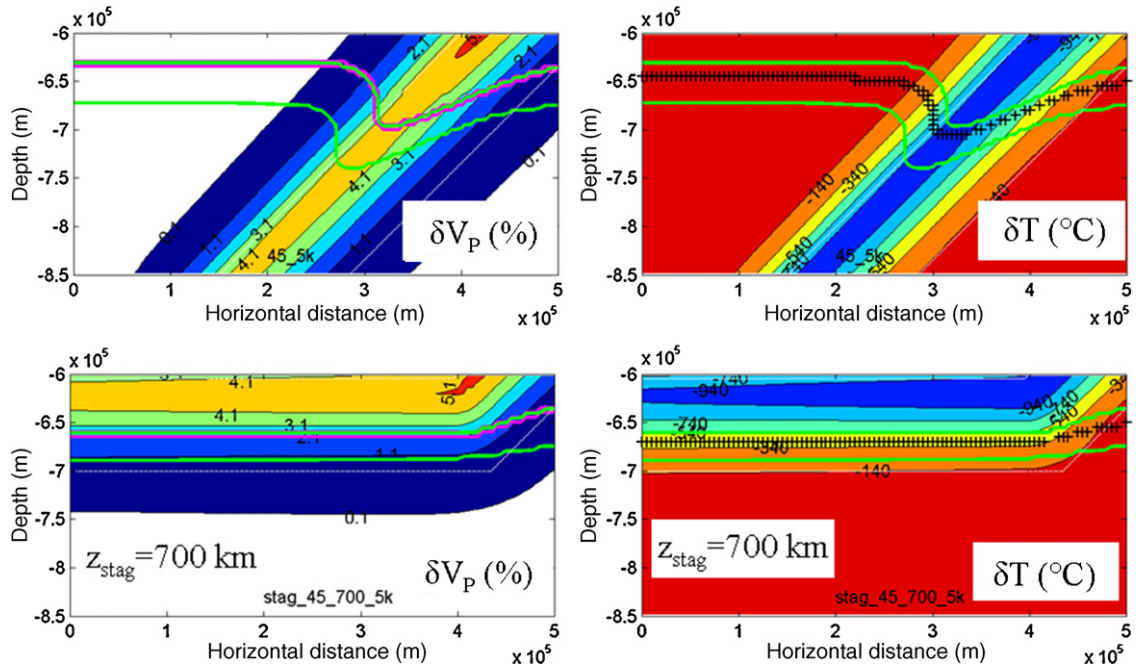
Fig. 10. Calculated perturbations to P-wave velocity δV_P (left) and temperature (right) for a penetrative slab (top) and a stagnant slab with z_{stag} = 700 km (bottom), as calculated using *TEMSPOL* (Negredo et al., 2004). Red/green lines show onset and completion of $rw \rightarrow pv + mw$ in simplified model of Schmeling et al. (1999); black crosses show univariant transition of Ito and Takahashi (1989). Note that penetrative slab yields discontinuity topography in agreement with receiver functions, and stagnant slab yields velocity anomlies in agreement with tomography. (For interpretation of the references to color in this figure legend, the reader is referred to the web version of the article.)
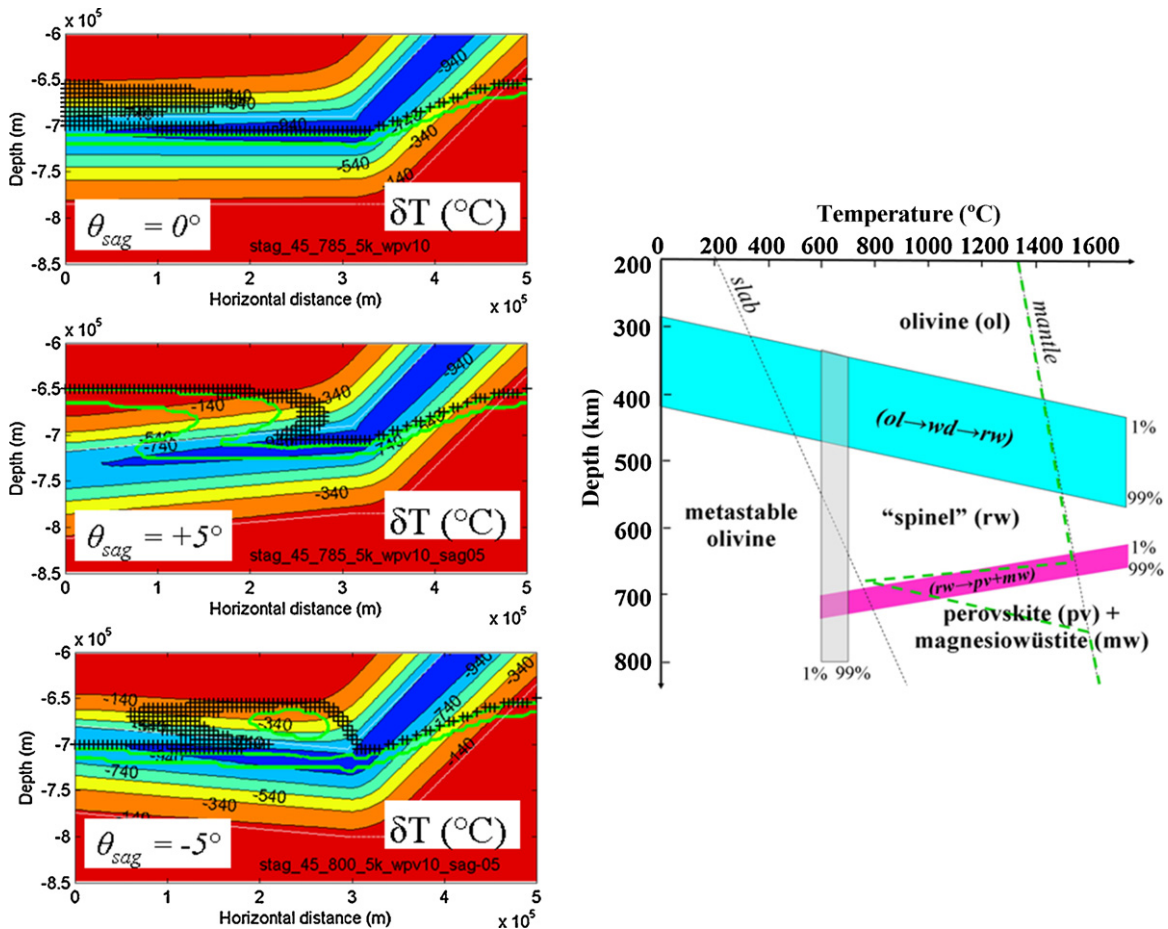

Fig. 11. Perturbations to temperature calculated using *TEMSPOL* (Negredo et al., 2004) for variations in post-stagnation dip angle θ_{sag} = 0° (top), +5° (middle), and −5° (bottom). Green lines show onset and completion of $rw \rightarrow pv + mw$ in simplified divariant model of Schmeling et al. (1999) as recalibrated for a narrower (10 km) transition thickness; black crosses show univariant (sharp) transition of Ito and Takahashi (1989). Note triplication of $rw \rightarrow pv + mw$ as the vertical temperature profile (green dashed) multiply intersects the transition (right). (For interpretation of the references to color in this figure legend, the reader is referred to the web version of the article.)

only for increasingly large values of the stagnation depth, perhaps too great to be consistent with tomographic images (Bina and Kawakatsu, 2005, 2006). How can these seemingly paradoxical observations be reconciled?

Might tomography underestimate depths to stagnant slab anomalies? Deeper penetration below 660 km (larger z_{stag}) would give the appearance of direct penetration through the transition zone and would provide larger bending moments to drive the stagnation of the slab, but it seems unlikely that tomographic analyses would so significantly underestimate the depth of fast velocity anomalies as to place them consistently in the transition zone rather than in the lower mantle. Might rapid thermal assimilation be the key? Swifter rebound of $rw \rightarrow pv + mw$ transition can be obtained if the slab warms dramatically (e.g., via shear heating) upon bending, but then the stagnant slab velocity anomaly should disappear from the tomography, too. Might crustal delamination play a role? A megalith-type model (Ringwood and Irifune, 1998) might achieve a superposition of penetrative and stagnant slab behavior, but a cold megalith would likely generate too broad a depression of the transition to match the receiver functions. Might trench rollback distort the images? Variations in trench rollback might allow some superposition of penetrative and stagnant subduction behavior. However, the cases illustrated by Christensen (2001) suggest additional complexity, such that either the $rw \rightarrow pv + mw$ transition should become depressed again at larger distances while the tomographic velocity anomaly undulates (his Fig. 2g) or the transition depression should be too broad as in the "megalith" case (his Fig. 2h).

Our modeling suggests a simpler reconciliation of the observations. A more penetrative-type rebound of a depressed $rw \rightarrow pv + mw$ transition is obtained if the stagnant slab "sags" slightly by a few degrees, rather than remaining strictly horizontal. We parameterize such variations in post-stagnation dip through the angle θ_{sag}, where a purely horizontal stagnant slab exhibits $\theta_{sag} = 0$, a positively dipping stagnant slab exhibits $\theta_{sag} > 0$ so that it continues to plunge shallowly into the lower mantle, and a negatively dipping stagnant slab exhibits $\theta_{sag} < 0$ so that it rebounds shallowly into the transition zone. Calculations for a small range of θ_{sag} values ($0° \pm 5°$) at large z_{stag} (785–800 km) suggest (Fig. 11) that a positive-dip stagnant slab, $\theta_{sag} = +5°$, can generate a swiftly rebounding $rw \rightarrow pv + mw$ transition similar to (although slightly laterally distorted from) that imaged in the receiver functions, but for such a geometry the bulk of the fast velocity anomaly associated with the slab (the boundaries of which will parallel the isotherms in the figure, as in Fig. 10) should reside in the lower mantle rather than the transition zone, and this is not consistent with the tomographic images.

On the other hand, a negative-dip stagnant slab, $\theta_{sag} = -5°$, can generate a swiftly rebounding $rw \rightarrow pv + mw$ transition similar to that imaged in the receiver functions, and the bulk of the fast velocity anomaly associated with the slab remains in the transition zone, consistent with the tomographic images. In this case, the transition may be deflected downward again several hundred kilometers downstream from the stagnation axis, if the slab ascends to intersect it once again (as opposed to eventually flattening out). Indeed, there are hints of just such a geometry – a slight upward bend prior to subsequent flattening — in the tomographic images. It is interesting to note that, for all three values of θ_{sag}, these calculations exhibit a "triplication" of the $rw \rightarrow pv + mw$ transition in stagnant slab, as the vertical temperature profile multiply intersects the transition.

Turning from these approximate models of the phase transitions to a full free-energy minimization, we can investigate the potential seismological visibility of these features. Firstly, we calculate perturbations in bulk sound velocity δV_Φ relative to a mantle reference model, for equilibrium mineralogy and $\theta_{sag} = -5°$, in an effort to approximate the view that might be formed through seis-

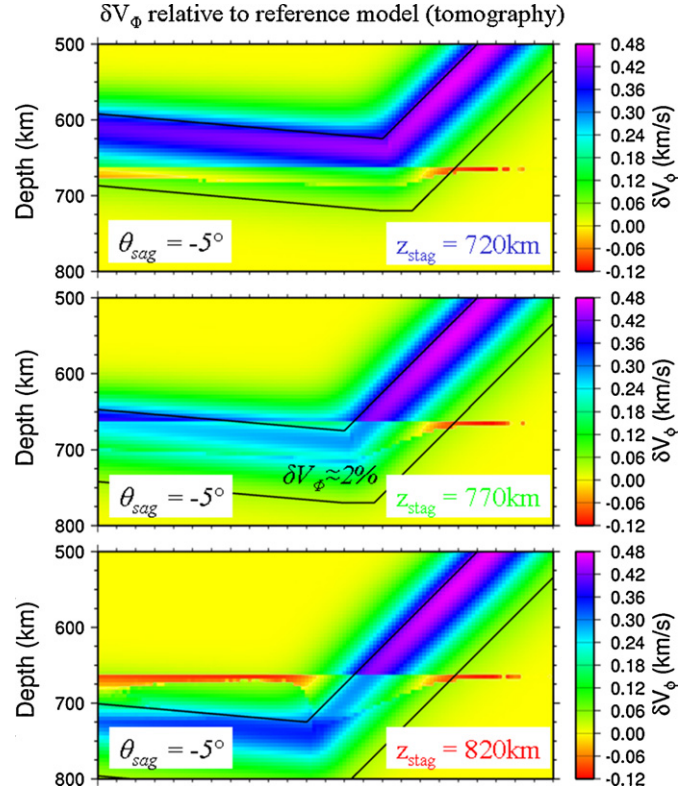**Fig. 12.** Calculated perturbations in bulk sound velocity δV_Φ relative to a reference model, to approximate imaging by seismic tomography, for varying depths of slab stagnation ($z_{stag} = 720$ km, 770 km, 820 km), where $\theta_{sag} = -5°$. Note that fast anomaly within transition zone remains at $\delta V_\Phi \approx 2\%$ and largely near 700–750 km.
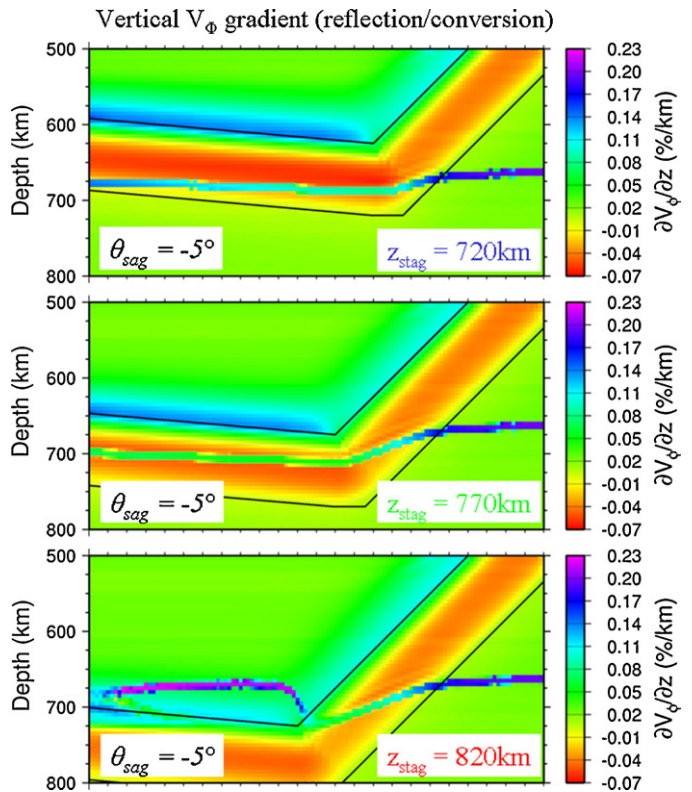

Fig. 13. Calculated (fractional) vertical gradients in bulk sound velocity $\partial V_\Phi/\partial z$, to approximate imaging by seismic reflections and conversions, for varying depths of slab stagnation ($z_{stag} = 720$ km, 770 km, 820 km), where $\theta_{sag} = -5°$. Note that for $770 < z_{stag} < 820$ km, the character of the transition achieves good agreement with receiver-function image.

mic tomography (Fig. 12). Here again, the broad, fast anomaly associated with the recumbent portion of the slab is damped and thinned for some values of z_{stag}, because the slab model features a depressed $rw \rightarrow pv + mw$ reaction while the reference model does not. Even for the maximum damping at $z_{stag} = 770$ km, however, the fast velocity anomaly within the transition zone remains at levels of $\delta V_\Phi \approx 2\%$, and for larger $z_{stag} = 820$ km the maximum depth of the slightly larger δV_Φ remains near 750 km, in broad agreement with tomographic images. Secondly, we calculate the (fractional) vertical gradient in bulk sound velocity $\partial V_\Phi / \partial z$, in an effort to approximate the view that might be formed through study of reflected and converted seismic phases (Fig. 13). Again, larger z_{stag} is associated with greater depression of the equilibrium $rw \rightarrow pv + mw$ reaction (from low slab temperatures). Furthermore, there is a significant decrease in the magnitude of the sharp vertical velocity gradient accompanying this reaction, as the narrow positive gradient is superposed upon a broader negative velocity gradient arising from the temperature structure within the slab. For z_{stag} approaching 820 km, however, the deflection, rebound, and sharpness of the transition all achieve good agreement with the receiver-function image. In particular, z_{stag} of 770 km exhibits partial ($\sim$50%) rebound over a horizontal distance of $\sim$500 km, and z_{stag} of 820 km rebounds over $\sim$225 km. The receiver functions indicate rebound over $\sim$400 km, suggesting an optimal $770 < z_{stag} < 820$ km for $\theta_{sag} = -5°$ (with shallower z_{stag} for steeper θ_{sag}).

Such a geometry corresponds to a category of results from dynamical simulations, such as those by Torii and Yoshioka (2007), that is intermediate between extremal buoyancy- and viscosity-dominated regimes and moderated by slight trench retreat (e.g., their Fig. 9d). Essentially, it appears that the phase-transition buoyancy component allows for primary stagnation below (rather than above) 660 km, while viscosity contrast and trench retreat together may contribute to the negative θ_{sag} (although the latter might also arise from kinetic effects not included in their dynamical models).

It is intriguing that our model of a slab stagnating with its upper surface initially penetrating below the $rw \rightarrow pv + mw$ reaction but above the $mj \rightarrow pv$ transition appears to be consistent with an independent model for formation of eclogitic diamond inclusions recently proposed by Harte (2009). It should be noted, however, that other receiver-function studies near our study region have noted broad depressions of the 660-km seismic discontinuity superimposed upon narrower, deeper depressions. Niu et al. (2005) interpreted such observations beneath southwest Japan as evidence for a stagnant slab lying either above or across the discontinuity. Ai et al. (2003) and Li and Yuan (2003) additionally interpreted similar observations beneath northeast China in terms of possible local penetration into the lower mantle of a generally neutrally buoyant stagnant slab, with Li and Yuan (2003) further suggesting a possible role for metastable olivine in local seismogenesis.

6. Non-olivine phases

All of the models presented thus far are based upon phase relations solely in olivine of Fo_{90} composition, encompassing the mineral phases olivine, wadsleyite, ringwoodite, silicate perovskite, and ferropericlase. The large volume fractions of these phases in mantle and slab peridotites, together with the generally sharp character of the phase transitions in this system, suggest that these phases should dominate the thermo-petrological effects on slab stagnation. Here, as an indication of future work, we briefly
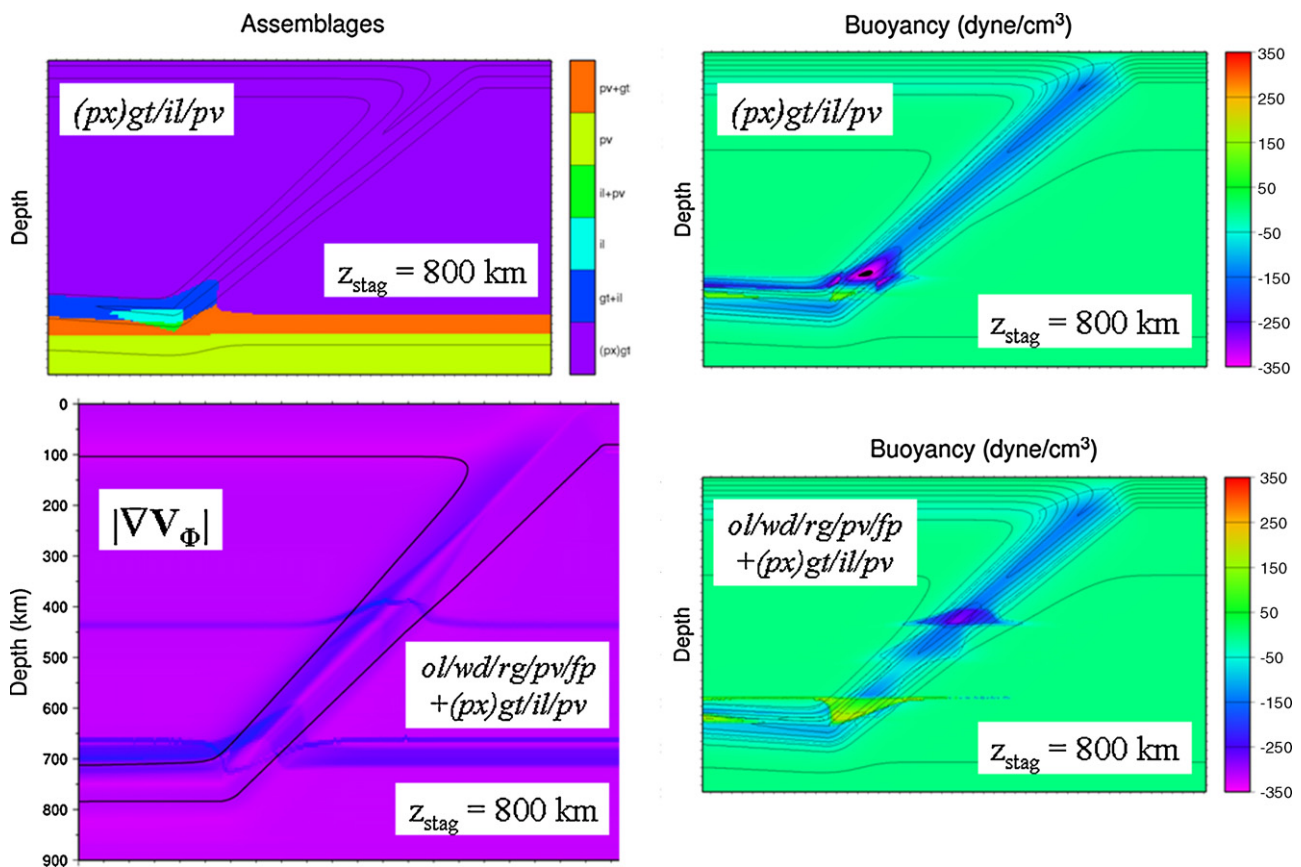

Fig. 14. Preliminary attempt to incorporate pyroxene, garnet, majorite, and akimotoite into models, for thermodynamics of Akaogi et al. (2002, 2003). Note stability field of coexisting garnet–majorite and akimotoite in recumbent portion of stagnant slab (top left), yielding negative buoyancy anomaly (top right), partially counteracting large positive buoyancy from depressed $rw \rightarrow pv + mw$ in pyrolite (bottom right). Broader character of pyroxene–garnet transitions perturbs seismic structure mostly at longer wavelengths (bottom left).

outline preliminary results which attempt to incorporate the non-olivine phases pyroxene, garnet, majorite, and akimotoite (silicate ilmenite) into slab models (Vacher et al., 1998). Incorporating the thermodynamics of these phase relations after Akaogi et al. (2002, 2003) into our free-energy minimization calculations yields some additional complexity, as the stability of a region of coexisting garnet-majorite and akimotoite in the recumbent portion of the stagnant slab adds a negative buoyancy anomaly which partially counteracts the large positive buoyancy anomaly associated with the depressed $rw \rightarrow pv + mw$ reaction (Fig. 14). The generally broader character of the phase transitions in this system, however, indicate that corresponding changes to seismic structure should occur primarily at longer wavelengths.

7. Summary

In summary, thermo-petrological buoyancy forces yield extrema near 700 km depth in the gradients of bending moments about the trench axis whose sign is consistent with a decrease in slab dip angle ("stagnation") at the base of the transition zone, as is observed in tomographic images and in patterns of deep seismicity. Bending moment gradients also exhibit extrema near 400 km depth whose sign is consistent with an increase in dip angle ("drooping"), as is sometimes observed in seismicity patterns below depths of 300 km. Any metastable persistence of low-pressure phases further enhances stagnation, to the extent that bending moments themselves become positive near 700 km depth, inhibiting direct slab penetration in such cases.

Variations in stagnation depth yield significant changes in bending moments (and their gradients) about the stagnation axis, ranging from small negative buoyancy anomalies in the recumbent portion of the slab (promoting downward deflection) to large positive buoyancy anomalies (promoting upward deflection), suggesting the existence of an equilibrium stagnation depth governed by the thermal state of the slab. Dip-dependence of buoyant bending moments suggests that slabs may overshoot their equilibrium stagnation depths before subsequently rebounding. Potential continuation of metastable persistence into the recumbent slab yields bending moment gradients that promote strong upward deflection, but this effect decays (due to thermal equilibration) over 600–700 km of lateral travel, thereafter yielding bending moment gradients consistent with downward deflection.

Both the vertical and lateral extent of downward deflection of the equilibrium $rw \rightarrow pv + mw$ transition (associated with the "660-km" seismic discontinuity) also exhibit dependence upon stagnation depth. Small values of z_{stag} yield shallow and broad depressions of the phase boundary, while larger values produce deep and broad depressions, and still larger values yield deep and narrow depressions similar to those expected for direct slab penetration. Stagnation depth further controls the seismological visibility of these effects through superposition of broad negative (vertical) velocity gradients upon the sharper $rw \rightarrow pv + mw$ transition, and any persistence of metastable phases may yield steeply dipping seismic reflectors within the slab.

Recent images derived from migrated receiver functions yield high-resolution constraints on the lateral depth variations of the 660-km seismic discontinuity beneath Japan, along an apparently stagnant slab as imaged by body-wave tomography. Models of slabs which penetrate the transition zone exhibit significant depression of the $rw \rightarrow pv + mw$ transition below 660 km, with swift rebound back to 660 km depth. Simple models of a stagnant slab, on the other hand, exhibit moderate depression of the $rw \rightarrow pv + mw$ transition, with spatially delayed rebound back to 660 km depth. Stagnant slab models more closely resemble the receiver-function images for increasingly large stagnation depths, but such large depths are not consistent with tomographic images. A good fit to both

receiver functions and tomography simultaneously is obtained at reasonable stagnation depths ($\sim$780–810 km) if the transition is moderately sharp and the stagnant slab initially bends upwards by a few degrees upon stagnating. In this case, a deep and relatively narrow depression of the $rw \rightarrow pv + mw$ transition is obtained, while the corresponding P-wave velocity anomaly is largely concentrated near 700 km depth. Such scenarios also result in triplication of the $rw \rightarrow pv + mw$ transition downstream of the stagnation point, as the geotherm passing through the stagnant slab multiply intersects the equilibrium phase boundary.

Preliminary efforts to incorporate pyroxene-garnet-akimotoite phases in these models suggest that these phase relations contribute moderate perturbations to the large buoyancy anomalies arising from olivine polymorphism and larger long-wavelength changes to seismic structure.

References

Ai, Y., Zheng, T., Xu, W., He, Y., Dong, D., 2003. A complex 660-km discontinuity beneath northeast China. Earth Planet. Sci. Lett. 212, 63–71.
Akaogi, M., Tanaka, A., Ito, E., 2002. Garnet–ilmenite–perovskite transitions in the system $Mg_4Si_4O_{12} - Mg_3Al_2Si_3O_{12}$ at high pressures and high temperatures: phase equilibria, calorimetry and implications for mantle structure. Phys. Earth Planet. Inter. 132, 303–324.
Akaogi, M., Tanaka, A., Ito, E., 2003. Erratum. Phys. Earth Planet. Inter. 135, 291.
Billen, M.I., 2008. Modeling the dynamics of subducting slabs. Ann. Rev. Earth Planet. Sci. 36, 325–356.
Bina, C.R., 1998a. Free energy minimization by simulated annealing with applications to lithospheric slabs and mantle plumes. Pure Appl. Geophys. 151, 605–618.
Bina, C.R., 1998b. A note on latent heat release from disequilibrium phase transformations and deep seismogenesis. Earth Planets Space 50, 1029–1034.
Bina, C.R., Kawakatsu, H., 2005. Slab stagnation depth: buoyancies, bending moments, and seismic structure. In: Abstr. 9th International Workshop on Numerical Modeling of Mantle Convection and Lithospheric Dynamics (IWMMCLD-9), Erice, Italy, pp. 13–14.
Bina, C.R., Kawakatsu, H., 2006. Seismological constraints on the thermal structure of the stagnant slab beneath Japan. In: Abstr. 5th Biennial Workshop on Subduction Processes in the Japan-Kurile-Kamchatka-Aleutian Arcs (JKASP-5), Sapporo, Japan, P513, 96.
Bina, C.R., Stein, S., Marton, F.C., Van Ark, E.M., 2001. Implications of slab mineralogy for subduction dynamics. Phys. Earth Planet. Inter. 127, 51–66.
Bina, C.R., Helffrich, G., 1994. Phase transition Clapeyron slopes and transition zone seismic discontinuity topography. J. Geophys. Res. 99, 15,853–15,860.
Brocher, T., Wells, R., Johnson, S., Weaver, C., Kirby, S., Pratt, T., Blakely, R., McCrory, P., 2001. Interaction of the slab, seismicity, and forearc basins in the Pacific northwest. In: Abstr. Earthscope Workshop: Making and Breaking a Continent, Snowbird, Utah, Southern California Earthquake Center.
Čížková, H., Čadek, O., Slancová, A., 1998. Regional correlation analysis between seismic heterogeneity in the lower mantle and subduction in the last 180 Myr: implications for mantle dynamics and rheology. Pure Appl. Geophys. 151, 527–537.
Čížková, H., van Hunen, J., van den Berg, A.P., Vlaar, N.J., 2002. The influence of rheological weakening and yield stress on the interaction of slabs with the 670-km discontinuity. Earth Planet. Sci. Lett. 199, 447–457.
Čížková, H., van Hunen, J., van den Berg, A.P., 2007. Stress distribution within the subducting slabs and their deformation in the transition zone. Phys. Earth Planet. Inter. 161, 202–214.

Chen, P., Bina, C.R., Okal, E.A., 2004. A global survey of stress orientations in subducting slabs as revealed by intermediate-depth earthquakes. Geophys. J. Int. 159, 721–733.

Chen, P., Bina, C.R., Okal, E.A., 2005. Erratum. Geophys. J. Int. 161, 419.

Chen, W., Tseng, T., Brudzinski, M., and Green, H.W., 2008. Petrologic anomalies in the mantle transition zone. Eos Trans. AGU, 89 (53), Fall Meet. Suppl., Abstr. DI13C-04.

Christensen, U., 2010. Geodynamic models of deep subduction. Phys. Earth Planet. Inter. 127, 25–34.

Fei, Y., Mao, H.-K., Mysen, B.O., 1991. Experimental determination of element partitioning and calculation of phase relations in the MgO–FeO–SiO$_2$ system at high pressure and high temperature. J. Geophys. Res. 96, 2157–2170.

Fukao, Y., Obayashi, M., Nakakuki, T., Deep Slab Project Group, 2009. Stagnant slab: a review. Ann. Rev. Earth Planet. Sci. 37, 19–46.

Fukao, Y., Widiyantoro, S., Obayashi, M., 2001. Stagnant slabs in the upper and lower mantle transition region. Rev. Geophys. 39, 291–323.

Gorbatov, A., Kostoglodov, V., 1997. Maximum depth of seismicity and thermal parameter of the subducting slab. Tectonophysics 277, 165–187.

Green, H.W., Zhou II, Y., 1996. Transformation-induced faulting requires an exothermic reaction and explains the cessation of earthquakes at the base of the mantle transition zone. Tectonophysics 256, 39–56.

Harte, B., 2009. Diamond formation in association with deep mantle dehydration zones. Eos Trans. AGU, 90 (52), Fall Meet. Suppl., Abstr. DI41CC-1820.

Ito, E., Takahashi, E., 1989. Postspinel transformations in the system Mg$_2$SiO$_4$ – Fe$_2$SiO$_4$ and some geophysical implications. J. Geophys. Res. 94, 10,637–10,646.

Karato, S., Riedel, M.R., Yuen, D.A., 1998. How strong are the subducted slabs? In: UMSI Research Report 98/113. Minnesota Supercomputer Institute, 29 pp.

Kawakatsu, H., 2008. Seismic imaging of meta-stable olivine wedge in the subducting slab beneath Japan via vectorial receiver function. Eos Trans. AGU, 89 (53), Fall Meet. Suppl., Abstr. S14C-03.

Kawakatsu, H., and Watada, S., 2005. Fine mapping of the mantle discontinuities beneath the Japanese islands using short-period Hi-Net data. Eos Trans. AGU, 86 (52), Fall Meet. Suppl., Abstr. DI41A-1248.

Kirby, S.H., Durham, W.B., Stern, L.A., 1991. Mantle phase changes and deep earthquake faulting in subducting lithosphere. Science 252, 216–225.

Kirby, S.H., Stein, S., Okal, E.A., Rubie, D.C., 1996. Metastable mantle phase transformations and deep earthquakes in subducting oceanic lithosphere. Rev. Geophys. 34, 261–306.

Kostoglodov, V.V., 1989. Maximal'naya glubina zemletryasenii i fazovye prevrashcheniya v litosfere, pograzhayushchejsya v mantiyu. In: Magnitskii, V.A. (Ed.), Fizika i vnutrennee stroienie zemli. Nauka, Moskva, pp. 52–57 (in Russian).

Kubo, T., Kaneshima, S., Torii, Y., and Yoshioka, S., 2008. Seismological and experimental constraints on metastable phase transformations and rheology of the Mariana slab. Eos Trans. AGU, 89 (53), Fall Meet. Suppl., Abstr. MR53A-1707.

Kubo, T., Ohtani, E., Kato, T., Urakawa, S., Suzuki, A., Kanbe, Y., Funakoshi, K., Utsumi, W., Kikegawa, T., Fujino, K., 2002. Mechanisms and kinetics of the post-spinel transformation in Mg$_2$SiO$_4$. Phys. Earth Planet. Inter. 129, 153–171.

Li, X., Yuan, X., 2003. Receiver functions in northeast China—implications for slab penetration into the lower mantle in northwest Pacific subduction zone. Earth Planet. Sci. Lett. 216, 679–691.

Minear, J.W., Toksöz, M.N., 1970. Thermal regime of a downgoing slab and new global tectonics. J. Geophys. Res. 75, 1379–1419.

Negredo, A.M., Valera, J.L., Carminati, E., 2004. TEMSPOL: A MATLAB thermal model for deep subduction zones including major phase transformations. Comput. Geosci. 30, 249–258.

Niu, F., Levander, A., Ham, S., Obayashi, M., 2005. Mapping the subducting Pacific slab beneath southwest Japan with Hi-net receiver functions. Earth Planet. Sci. Lett. 239, 9–17.

Ringwood, A.E., Irifune, T., 1998. Nature of the 650-km seismic discontinuity—implications for mantle dynamics and differentiation. Nature 331, 131–136.

Schmeling, H., Monz, R., Rubie, D.C., 1999. The influence of olivine metastability on the dynamics of subduction. Earth Planet. Sci Lett. 165, 55–66.

Sugioka, H., Suetsugu, D., Obayashi, M., Fukao, Y., Gao, Y., 2010. Fast P and S wave velocities associated with the "cold" stagnant slab beneath the northern Philippine Sea. Phys. Earth Planet. Inter. 179, 1–6, doi:10.1016/j.pepi.2010.01.006.

Tetzlaff, M., Schmeling, H., 2000. The influence of olivine metastability on deep subduction of oceanic lithosphere. Phys. Earth Planet. Inter. 120, 29–38.

Torii, Y., Yoshioka, S., 2007. Physical conditions producing slab stagnation: constraints of the Clapeyron slope, mantle viscosity, trench retreat, and dip angles. Tectonophysics 445, 200–209.

Vacher, P., Mocquet, A., Sotin, C., 1998. Computation of seismic profiles from mineral physics: the importance of the non-olivine components for explaining the 660 km depth discontinuity. Phys. Earth Planet. Inter. 106, 275–298.

Wessel, P., Smith, W.H.F., 1998. New, improved version of generic mapping tools released. Eos Trans. Am. Geophys. U. 79 (47), 579.

Widiyantoro, S., Kennett, B.L.N., van der Hilst, R.D., 1999. Seismic tomography with P and S data reveals lateral variations in the rigidity of deep slabs. Earth Planet. Sci. Lett. 173, 91–100.

Yoshioka, S., Daessler, R., Yuen, D.A., 1997. Stress fields associated with metastable phase transitions in descending slabs and deep-focus earthquakes. Phys. Earth Planet. Inter. 104, 345–361.